Molecular interactome of HNRNPU reveals regulatory networks in neuronal differentiation and DNA methylation

AUTHORS

Marika Oksanen[1,2,3], Francesca Mastropasqua[1,2], Krystyna Mazan-Mamczarz[3], Jennifer L. Martindale[3], Xuan Ye[1,2], Abishek Arora[1,2], Nirad Banskota[3], Myriam Gorospe[3], Kristiina Tammimies[1,2*]

[1]Center of Neurodevelopmental Disorders (KIND), Centre for Psychiatry Research, Department of Women's and Children's Health, Karolinska Institute, Region Stockholm, Stockholm, Sweden.

[2]Astrid Lindgren Children's Hospital, Karolinska University Hospital, Region Stockholm, Stockholm, Sweden.

[3]Laboratory of Genetics and Genomics, National Institute on Aging Intramural Research Program, National Institutes of Health, Baltimore, Maryland, USA.

* To whom correspondence should be addressed. Tel: +46 76 237 9741 Email: kristiina.tammimies@ki.se

ABSTRACT

HNRNPU is an RNA-binding protein with diverse roles in regulating gene expression. Pathogenic genetic variants of HNRNPU cause a severe neurodevelopmental disorder (NDD), but the underlying molecular mechanisms are unclear. Here, we investigated the protein-protein interaction (PPI) network and RNA targets of HNRNPU in neuroepithelial stem cells (NES) and differentiating neural cells derived from human induced pluripotent stem cells. Using high-throughput approaches, we found HNRNPU interacting with the mammalian SWI/SNF complex and highlight its putative role in multiple stages of mRNA regulation. Notably, both PPI partners and interacting mRNAs implicated HNRNPU in translation, a role that had not been recognized before. Also, we found that HNRNPU associated with mRNAs encoding proteins important for neuronal development. Based on our findings, we propose a regulatory model in which HNRNPU, in coordination with SWI/SNF, modulates the levels and accessibility of DNA methylation factors, leading to global methylation differences in HNRNPU deficiency states, as we validated in our cell model. This mechanism provides a molecular link to the distinct methylation signature seen in individuals with HNRNPU-related NDDs as well as to crucial epigenetic regulation during early brain development.

INTRODUCTION

Heterogeneous nuclear ribonucleoprotein U (HNRNPU), also known as scaffold attachment factor A (SAF-A), is a multifunctional protein critical for RNA metabolism and chromatin organization. HNRNPU facilitates open chromatin conformation, particularly at active promoters (1, 2). Moreover, its binding near transcription start sites has been shown to increase transcriptional activity in breast cancer cell lines (3). Beyond its chromatin-related roles, HNRNPU interacts with diverse RNAs to regulate post-transcriptional processes such as RNA stabilization, splicing, and nonsense-mediated decay (4–9). In neural cells, it has been shown that HNRNPU regulates chromatin compaction, gene expression, and alternative splicing, suggesting a critical role in neural development and function (10–13). HNRNPU has also been identified in RNA-transporting granules in both human and mouse neurons (14, 15), and lowering HNRNPU levels by silencing in mouse hippocampal neurons impairs RNA transport (14).

Haploinsufficiency of *HNRNPU* causes severe neurodevelopmental disorders (NDD), collectively known as HNRNPU-related NDDs, in which the affected individuals have general developmental delay, intellectual disability (ID), autism spectrum disorder (ASD), and epilepsy, among other features (16–18). Similar phenotypes have been reported in individuals having pathogenic genetic variants in other HNRNP family proteins(19). Expanding upon the genetic findings, recent epigenomic analyses have identified distinct blood DNA methylation differences in individuals with HNRNPU-related NDDs(20, 21). These findings of widespread alterations in methylation patterns suggest that chromatin dysregulation leading to methylation changes could be one of the key molecular mechanisms underlying the phenotypes seen in HNRNPU-related NDDs. The differences could then drive the changes observed in neuronal progenitor survival and differentiation earlier indicated as the key mechanisms leading to the brain phenotypes (10, 11, 13).

Efforts to define the molecular interactome of HNRNPU have identified RNA targets via techniques such as ribonucleoprotein immunoprecipitation followed by RNA sequencing (RIP-Seq), formaldehyde crosslinking followed by RIP-Seq (fRIP-Seq) and enhanced cross-linking immunoprecipitation sequencing (eCLIP/CLIP-Seq) analyses in diverse cell types and tissues, including human hepatocellular carcinoma, embryonic kidney, leukemia, HeLa and pluripotent stem cell lines, as well as adrenal gland tissue (4, 22–25). Additionally, two

screenings to identify protein-protein interaction (PPI) partners of HNRNPU have been performed in breast cancer cell line and mouse testis tissue (3, 26). Furthermore, HNRNPU has been shown to interact with multiple proteins, such as other HNRNP family members in spliceosome complexes (27). Yet, a comprehensive profiling of interacting proteins in neural cells has been lacking as previous work has focused on the effects of HNRNPU deficiency on transcriptomic changes in human neural 2D and 3D culture models (10, 11) and mouse models (12, 13). Here, we investigated the molecular interactome, RNA targets, and PPI partners of HNRNPU in human neural development using induced pluripotent stem cells (iPSCs)-derived neural cells. Furthermore, we validate key interactions and their effects in a HNRNPU deficiency state, including global methylation changes. Through this comprehensive approach, we sought to elucidate the molecular pathways disrupted in HNRNPU-NDD models (10–13), and to understand better the mechanisms underlying the phenotypes associated with HNRNPU-related NDDs.

MATERIAL AND METHODS

Cell culture

The cell lines used in this study were previously established and characterized human iPSC lines derived from a neurotypical male (CTRL9-II (28), hereafter $CTRL_{Male}$) and a neurotypical female (AF22 (29), hereafter $CTRL_{Female}$). Both cell lines had been previously induced into neuroepithelial stem (NES) cells (29, 30).

For the experiments, NES cells were seeded on 20 µg/mL poly-L-ornithine (Sigma Aldrich), and 1 µg/mL laminin (Sigma Aldrich) coated surfaces in DMEM/F12 + Glutamax medium (Gibco) with 0.05X B-27 (Gibco), 1X N-2 (Gibco), 10 ng/mL bFGF (Life Technologies), 10 ng/mL EGF (PeproTech) and 10 U/mL penicillin/streptomycin (Gibco), with daily media changes. For immunofluorescence, coverslips were coated with 100 µg/mL poly-L-ornithine and 2 µg/mL laminin. Cells were maintained in 5% CO_2 at 37°C. NES cells were differentiated into neurogenic cultures using an undirected differentiation protocol, with media containing 0.5X B-27 and 0.4 µg/mL laminin without bFGF and EGF, with media changes every other day until day 15, then every third day. Cells were harvested at differentiation days 0 (NES, D0), 7 (D7), 14 (D14) and 28 (D28).

Formaldehyde crosslinking and ribonucleoprotein immunoprecipitation

Formaldehyde crosslinking and ribonucleoprotein immunoprecipitation (fRIP) was performed at D0 and D28, followed by mass spectrometry (IP-MS) or RNA sequencing (fRIP-Seq) analysis. Formaldehyde crosslinking was performed as described earlier (23) with modifications. Cells were washed with DPBS, dissociated with TrypLE Express (D0) or Accutase and TrypLE Select and incubated with Neural Isolation Enzyme (D28), and resuspended in Wash medium (DMEM/F12+GlutaMAX, 5% FBS, 10 U/mL penicillin/streptomycin). Cells were gently resuspended and spun at 400 × *g* for 3 min and resuspended in Wash medium or 1 mL of PBS, supplemented with 0.15 % Triton-X and 30 µL RNase A (Sigma, R4642) to degrade all RNA as described earlier(31). Cells were counted, and wash media was added to $5x10^6$ cells/mL concentration. Cells were crosslinked with 0.1% formaldehyde for 10 min with rotation at room temperature, the reaction was stopped with 125 mM glycine for 5 min with rotation at room temperature, and washed twice in cold DPBS with 1x Halt protease inhibitor cocktail (PIC, Thermo Scientific). Cell pellets were stored at -80°C.

Cell lysis and protein immunoprecipitation were performed following an existing protocol (32) with modifications. Shortly, cell pellets were lysed in polysome lysis buffer (PLB, 100 mM KCL, 5 mM $MgCl_2$, 10 mM HEPES (pH 7.0), 0.5% IGEPAL, 1 mM DTT, 100 units/mL RNaseOUT, 1xPIC). The cell lysate was incubated on ice for 10 min before centrifugation at 10,000 × *g* at 4°C. The lysate was transferred to a fresh microfuge tube and pre-cleared by incubating with Dynabeads Protein G (Life Technologies) with 25 µL of beads per sample for 30 min at 4°C with slow rotation. For fRIP-Seq, 5% of the sample was removed for input and stored at -80°C. Protein concentrations were measured using Pierce BSA protein assay kit (Thermo Scientific) and an equal protein amount of lysate was divided into two microfuge tubes per replicate, 1.5 and 1 mg for fRIP-Seq and IP-MS, respectively and NT-2 buffer (50 mM Tris (pH 7.4), 150 mM NaCl, 1 mM $MgCl_2$, 0.05% IGEPAL, 1 mM DTT, 400 units/mL RNaseOUT, 16.5 mM EDTA) was added to final volume 1 mL. Either the HNRNPU antibody (ab20666, Abcam) or rabbit IgG (12-370, Sigma-Aldrich) was added at a concentration of 7 µg per 1 mg of total protein, and the reactions were incubated for 2 h at 4°C with rotation. Dynabeads protein G was prepared according to the manufacturer's instructions, and 50 µL per 1 mg of total protein was added to fRIP-Seq and IP-MS tubes, respectively. The incubation was prolonged for 1 h. The beads were washed thrice with 1 mL ice-cold NT-2 buffer, rotating for

10 min at 4°C. After a final wash, the supernatant was removed, and beads were stored at -80°C.

Mass spectrometry and analysis

Mass spectrometry was performed on $CTRL_{Male}$ samples. The beads-bound proteins were reduced in 1 mM DTT at room temperature for 30 min. Next, samples were alkylated by incubation in the dark at room temperature in 5 mM chloroacetamide for 10 min. After incubation, the remaining chloroacetamide was quenched by adding 5 mM DTT. Digestion was carried out by adding 0.4 µg Trypsin (sequencing grade modified, Pierce) and overnight incubation at 37°C. The next day the supernatant was collected and cleaned by a modified SP3 protocol (33). Briefly, 20 µL Sera-Mag SP3 bead mix (10 µg/µL) was added to the sample. Next, 100% acetonitrile was added to achieve a final concentration of >95%. Samples were pipette-mixed, incubated for 30 min at room temperature, and then placed on a magnetic rack. The supernatant was aspirated and discarded, and the beads were washed twice in 200 µL of acetonitrile. Samples were removed from the magnetic rack, and beads were reconstituted in 20 µL phase A (97% water, 3% acetonitrile, 0.1% formic acid). Then, the beads were placed on a magnetic rack again, and the supernatant was recovered and transferred to an MS-vial. Q-Exactive Online LC-MS (LC-ESI-MS/MS) was performed using a Dionex UltiMate™ 3000 RSLCnano System coupled to a Q-Exactive mass spectrometer (Thermo Scientific); 7 µL was injected from each sample. Samples were trapped on a C18 guard desalting column (Acclaim PepMap 100, 75 µm x 2 cm, nanoViper, C18, 5 µm, 100 Å) and separated on a 50-cm long C18 column (Easy spray PepMap RSLC, C18, 2 µm, 100Å, 75 µm x 15 cm). The nano capillary solvent A was 95% water, 5% DMSO, and 0.1% formic acid; solvent B was 5% water,5% DMSO, 95% acetonitrile, and 0.1% formic acid. At a constant flow of 0.25 µl min^{-1}, the curved gradient went from 6% B up to 43% B in 180 min, followed by a steep increase to 100% B in 5 min. FTMS master scans with 60,000 resolution (and mass range 300-1500 m/z) were followed by data-dependent MS/MS (30 000 resolution) on the top 5 ions using higher energy collision dissociation (HCD) at 30% normalized collision energy. Precursors were isolated with a 2 m/z window. Automatic gain control (AGC) targets were $1x10^6$ for MS1 and $1x10^5$ for MS2. Maximum injection times were 100 ms for MS1 and MS2. The entire duty cycle lasted ~2.5 s. Dynamic exclusion was used with 60 s duration. Precursors with unassigned charge state or charge state 1 were excluded. An underfill ratio of 1% was used. The MS raw files were

searched using Sequest-Percolator or Target Decoy PSM Validator under the software platform Proteome Discoverer 1.4 (Thermo Scientific) against human database and filtered to a 1% FDR cut off. We used a precursor ion mass tolerance of 15 ppm, and product ion mass tolerances of 0.02 Da for HCD-FTMS. The algorithm considered tryptic peptides with maximum 2 missed cleavage; carbamidomethylation (C) as fixed modifications; oxidation (M) as variable modifications.

For statistical analysis, only proteins identified by at least one peptide in two biological replicates were included. All keratins, histones, and immunoglobulins were considered contaminants and excluded. Significant HNRNPU-interacting proteins were selected based on FC > 2 and a Benjamini-Hochberg adjusted p-value <0.05 following a Student's t-test. Novel interactions were identified by comparing the identified PPI list with the BioGRID database for HNRNPU interactions (accessed January 2024). Proteins were clustered using the Markov Cluster Algorithm (MCL) within the STRING database in Cytoscape (34) (v.3.9.1). Gene Ontology (GO) enrichment analysis on biological processes (BP) or cellular components (CC) was performed using online tool WebGestalt (35) on each cluster to identify their functional relevance, and we reported the highest significant enrichment. AlphaPulldown python package (36) (v.1.0.4), which internally uses Alphafold2 (37) was used to predict the probability of HNRNPU forming a complex with the given proteins. The input to AlphaPulldown was a compiled list of proteins pulled down with IP-MS from D0 and D28 time points. We next used the run_get_good_pae.sh command to compile a list of hits and filtered further by considering only those with interface predicted template modeling (ipTM) score > 0.6 as significant.

RNA sequencing and analysis

fRIP-Seq was performed on samples from both $CTRL_{Male}$ and $CTRL_{Female}$ cell lines at D0 and from $CTRL_{Male}$ at D28. Beads and input samples were subjected to reverse crosslinking. The beads were resuspended to 56 µL Ultra Pure water and 33 µL of reverse crosslinking buffer (PBS--, 6% N-lauroyl sarcosine, 30 mM EDTA, 7.5 mM DTT), 10 mL of Proteinase K and 1 mL of RNaseOUT were added. After incubation (1 h at 42°C then 1 h at 55°C), samples were transferred to 500 µL TRIzol for RNA extraction, including DNA digestion. An equal amount of RNA, 18 ng, was used for library preparation with Illumina Stranded Total RNA Prep with Ribo-Zero Plus, and sequencing was run with Nextseq 200, P2, and 100 cycles.

RNA-seq reads were trimmed with bbduk of bbmap (v.39.01) and mapped to Homo Sapiens CRCh38 Ensembl 109 with STAR (38) (v.2.7.9a). Ribosomal reads and PCR duplicates were removed using BEDtools (v.2.31.1) intersecting with CHRCh38_rRNA.bed file (RSeQC) and Samtools (v.1.2) markdup -r, respectively. These files were subjected to CLAM (39) (v1.2.0) preprocessing, after which the peaks were called using only the uniquely mapped reads and bin size 100, read-tagger-method median, --unique-only TRUE, and –pool TRUE. Subsequent peak files were annotated with CLAM peak annotator, and resulting files were imported to R (v.4.3.2) for significance filtering. Genes with at least two peaks (adjusted $p < 0.05$) were considered significant HNRNPU targets. Enrichment of IP samples versus Input samples was analyzed using DESeq2 (40) (v.1.42.1). RNA count matrix was obtained from BAM files using Rsubread (41) (v.2.16.1). Differential expression was called using *design = ~ Cell_Line + Status* at D0 and *design = ~ Status* at D28, status including the information whether the sample was HNRNPU-IP or Input. A significantly enriched RNA target was called with log2FC > 1, adjusted p-value < 0.05, and base expression mean > 20. The identified RNA targets were compared with HNRNPU targets from other experiments, including fRIP-Seq performed in K562 cells (23), CLIP-Seq performed in HeLa cells (22), K562 (Encode accession ENCSR520BZQ), and HepG2 (Encode accession ENCSR240MVJ) cells as well as adrenal gland tissue (Encode accession ENCSR368GER). The compiled list of HNRNPU targets from CLIP-Seq was downloaded from the POSTAR3 database (42). Furthermore, we compared our HNRNPU targets with our earlier RNA-seq dataset (10) (available in GEO with GSE229004), which included genes that were differentially expressed and differentially spliced in response to HNRNPU deficiency, either in a patient cell line (HNRNPUdel) or following *HNRNPU* silencing (siHNRNPU). Additional comparisons were made to external datasets, including human HNRNPU CRISPR-Cas9 mutant cortical organoids (11), and conditional *Hnrnpu* mutant mouse model (13).

Enrichment analyses

Expression-weighted cell-type enrichment (EWCE) analysis was performed using the EWCE package (43) (v.1.10.2) and a human neocortical mid-gestation single cell RNA-Seq (scRNA-Seq) dataset as a reference (44). The reference scRNA-Seq dataset included samples from four donors, two of which were used for this analysis. The input gene lists were either IP-MS proteins or fRIP-seq RNA targets from D0 and D28 time points separately.

Gene set enrichment analysis (GSEA) was performed using the gprofiler2 package (45) (v0.2.3) in R for gene ontology biological processes. The input gene lists were either IP-MS proteins or fRIP-seq RNA targets from D0 and D28 time points separately, and the background was set to all expressed genes (BaseMean > 20) at respective time points based on our previous RNA-seq data (10). Significant enrichment was defined as FC > 1 and adjusted p-value < 0.05. For visualization, only terms with <500 annotated genes were shown.

Furthermore, hypergeometric tests were performed to assess enrichment between HNRNPU PPI proteins or RNA targets and specific NDD-related gene lists: ASD (SFARI genes selected for score 1,2 and syndromic, release 08-19-2024), ID (green and amber genes from https://panelapp.genomicsengland.co.uk/ v7.0) and epilepsy (green and amber genes from https://panelapp.genomicsengland.co.uk/ v6.0). For motif enrichment analysis for RNA targets from fRIP-seq data, the adjacent CLAM peak regions were collapsed with BEDTools (v2.31.0) intersect function, and the enrichment analysis was performed with SEA function of MEME-Suite (46) (v.5.5.7) with default settings and background as shuffled input sequences. The motifs for analysis were extracted from MEME-Suite and RBPMap (v1.2) and consolidated into a list of 237 motifs from 132 proteins (Supplementary Table 1).

Immunocytochemistry and proximity ligation assay

$CTRL_{Male}$ cells on glass coverslips at D0 were fixed in 4% formaldehyde for 20 min at room temperature or with ice-cold methanol for 10 min. Coverslips were washed with 1xDPBS. For immunofluorescence, blocking was performed with 5% donkey serum and 0.1% Triton X-100 in 1xDPBS for 1 h at room temperature. Primary antibodies [HNRNPU (Santa Cruz Biotechnology, sc-32315, 1:25), HNRNPU (Novus Bio, NBP2-49290, 1:500), FUS (Cell Signaling Technology, 67840S, 1:1000), ARID1B (Cell Signaling Technology, 92964S, 1:1000), EEF2 (Proteintech, 20107-1-AP, 1:500), NUFIP2 (Proteintech, 67195-1-Ig, 1:1000), DDX17 (Novus Bio, NB200-352, 1:500)] were diluted in blocking buffer and incubated overnight at +4°C. After washing with 1xDPBS, secondary antibodies (Anti-Mouse 555 (Biotium), and Anti-Rabbit 488 (Invitrogen)) diluted 1:1000 and Hoechst (1:2000, Invitrogen) in blocking buffer were incubated 1 h at room temperature, protected from light. Coverslips were washed with 1xDPBS and mounted with Diamond Antifade Mountant (ThermoFisher Scientific).

The in-situ proximity ligation assay (PLA) was performed using the Duolink PLA assay kit (Sigma) with In Situ Detection Reagents Red (Sigma), following the manufacturer's

instructions. After fixation, the cells were permeabilized with 0.1% Triton in DPBS for 15 min at room temperature, blocked with supplied blocking solution for 1 h at 37°C, and incubated with primary antibodies as above. Coverslips were incubated with secondary probes (anti-mouse-PLUS and anti-rabbit-MINUS) for 1 h at 37°C, ligation solution for 30 min at 37°C and amplification solution for 100 min at 37°C, with careful washing between steps. Coverslips were mounted with Duolink in Situ Mounting Medium with DAPI. Images were acquired using LSM 900 Zeiss Confocal Microscopes using 20x or 43x magnification or LSM 980 Zeiss Confocal Microscope using 63x magnification in Airyscan mode.

siRNA-mediated silencing

To silence *HNRNPU*, NES cells were seeded in 31,500 cells/cm^2, left to adhere for 4 h, and transfected with 1 µM Accell SMARTpool siRNA targeting *HNRNPU* mRNA (Dharmacon E-013501-00-0010) or Accell Nontargeting siRNA (Dharmacon D-001950-01-20) according to manufacturer's protocol. The *HNRNPU* siRNA pool consisted of the following oligos: oligo1: UCUUGAUACUUAUAAUUGU, oligo2: CUCGUAUGCUAAGAAUGGA, oligo3: GUUUCAGGUUUUGAUGCUA, oligo4: CUAGUGUGCUUGUAGUAGU. Transfected NES cells were harvested 72 h later. Cells under differentiation were transfected once in the NES phase, once when changing media to differentiation media, once on day 4 of differentiation, and collected on day 7 of differentiation.

Subcellular fractionation and Western blot analysis

For total protein extraction, cells were lysed in a buffer containing 2% sodium dodecyl sulfate (SDS) in 50 mM HEPES and sonicated at 37% amplitude (Vibra-Cell VCX-600, Sonics). Subcellular fractionation was performed using the PARIS kit (Invitrogen) at differentiation days 0, 7, and 14 using $CTRL_{Male}$ cells. Protein concentrations were measured with a Pierce BCA assay kit (Thermo Scientific). The resulting fractions were analyzed by western blot. Proteins (10 µg for total lysates and 1 µg for fractionated samples) were separated on 4-15 % gradient gels (Bio-Rad) and transferred onto nitrocellulose membranes using the Bio-Rad Turbo transfer system.

Membranes were blocked in 5% milk in TBS-Tween (0.1%) for 1 h at room temperature and incubated overnight with primary antibodies. The primary antibodies used were HNRNPU (Santa Cruz Biotechnology, sc-32315, 1:1000), Lamin B1 (Abcam, ab16048, 1:3000), GAPDH

(Invitrogen, 39-8600, 1:50000), TET1 (Novus Bio, NBP2-15135 1:200) and TET3 (Proteintech, 27150-1-AP, 1:1000). After three 10-min washes in TBS-Tween at room temperature, membranes were incubated with HRP-conjugated secondary antibodies (Cell Signaling Technology: anti-mouse 7076P2, 1:2000; anti-rabbit 7074P2, 1:2000) for 1 h at room temperature. Blots were visualized using the Pierce ECL Blotting Substrate, with a 2-min incubation time, and imaged using the Bio-Rad imaging system. Western blot quantification was performed using the Fiji ImageJ software and standard densitometry techniques.

Capillary Western blot analysis

The total protein samples (150 ng/μL) were loaded on the capillary western blot system Simple-Western-JESS (BioTechne), multiplexed for total protein and chemiluminescence detection of HNRNPU (1:50000 dilution), QSER1 (Novus Bio, NBP1-19112, 1:5 dilution), DNMT1 (Novus Bio, NB100-56519, 1:50), DNMT3A (Santa Cruz Biotechnology, sc-373905, 1:10), and DNMT3B (Santa Cruz Biotechnology, sc-376043, 1:100). Data were analyzed using Compass for S.W. software (5.0.1), and the peak areas were normalized against the total protein area. Three biological replicates were analyzed for each time point, and the Student's t-test was used to evaluate the significance at each time point.

RNA stability assay

To measure mRNA stability, NES cells were treated with siRNA, as described above. After 72 h of siRNA treatment, either DMSO or RNA polymerase II inhibitor actinomycin D (Sigma-Aldrich) in 5 μg/mL were added to the cells. Samples in DMSO were collected after 2 h (serving as the 0 h sample), and samples in Actinomycin D were collected in TRIzol after 2, 4, 6 or 8 h for RT-qPCR analysis. Three biological replicates were analyzed.

Polysome profiling

Cells were incubated for 3 min with 0.1 mg of cycloheximide/mL at 37°C and then lysed in 1 mL of PEB lysis buffer (20 mM Tris-HCl [pH 7.5], 0.1 M KCl, 5 mM MgCl2, 0.5% Igepal CA-630 with RNase and protease inhibitors) as well as 0.1 mg of cycloheximide/mL to interrupt protein translation and thus prevent the disassembly of polysomes "running off" of a given mRNA. After a 10-min incubation on ice, nuclei were pelleted by centrifugation at 10,000 × *g* for 10 min at 4°C, and the supernatant was carefully layered onto a 10-to-50% linear sucrose gradient.

Gradients were centrifuged at 39,000 rpm for 1.5 h at 4°C, and 1 mL fractions were collected using a system comprising a syringe pump, needle-piercing system (Brandel, Gaithersburg, MD), UV-6 detector, and fraction collector (ISCO, Lincoln, NE). The fractions were divided in half for protein samples and RNA samples (mixed with 0.5 mL TRIzol).

RNA extraction and reverse transcription (RT) followed by quantitative (q)PCR analysis

Cells lysed in TRIzol reagent (Invitrogen) were phase-separated using chloroform and isopropanol. The aqueous phase was transferred to RNA extraction columns, and the final extraction was carried out with ReliaPrep RNA Cell Miniprep kit (Promega Z6012). The RNA was reverse transcribed using iScript cDNA Synthesis Kit (BioRad) and cDNA quantified with SsoAdvanced Universal SYBR Green Supermix (BioRad) following the manufacturer's protocols on a CFX384 Touch Real-Time PCR Detection System (Bio-Rad). The primers used are listed in Supplementary Table 2. We used three biological replicates of cells seeded at different cell passages and reactions for each sample were performed in three technical replicates. CFX Manager software was used to record amplification curves to determine Ct values. We used three biological replicates of cells seeded at different passages. In mRNA stability assays, we calculated ΔCt relative to the levels of *GAPDH* mRNA, and ΔΔCt to samples incubated with DMSO without Actinomycin D, for determining percentage of remaining mRNA at each time point. mRNA decay curves were modelled using polynomial regression with second-degree polynomial formula. The slope of the curve was used to determine half-life of the mRNAs. For polysome profiling, the percent distribution for the mRNAs across the gradients was calculated using the ΔCT method.

DNA extraction and global 5mC DNA methylation assay

DNA was extracted after HNRNPU silencing using the PureLink Genomic DNA Mini kit following the manufacturer's instructions. Global 5mC DNA methylation was measured using the Methylflash ELISA Easy Kit (Colorimetric, Epigentek) according to the manufacturer's instructions with 100 ng of DNA loaded in duplicates. The experiments were performed in three biological replicates and significance was determined with the Student's t-test.

Statistical analysis

Statistical analyses were performed using R (v.4.3.2) and details for specific statistics are explained in the respective methods sections.

RESULTS

HNRNPU protein partner screen identifies six protein networks in neural cells and highlights its involvement in translation dynamics

To identify PPI partners of HNRNPU in NES at days 0 and 28 (D0 and D28), we performed HNRNPU IP (Supplementary Figure S1A) followed by LC-ESI-MS/MS detection of the protein lysates, without or with RNase treatment (hereafter referred as direct interactions). We identified 244 interacting proteins at D0 and 79 at D28 (Figure 1A, Supplementary Table 3). Among these, 72 (30.0%) and 16 (20.3%) proteins were identified as direct interactions at D0 and D28, respectively, with 13 proteins shared between both time points. When comparing our data with the BioGRID database (downloaded January 2024), we identified 54 novel direct interacting partners of HNRNPU. Analysis of the proteins dissociated after RNase treatment revealed that 172 and 63 proteins interacted with HNRNPU in an RNA-dependent manner at D0 and D28, respectively, with 31 common to both time points. Of these, 92 represented novel PPIs with HNRNPU. In total, 112 of the known PPIs of HNRNPU are RNA-assisted rather than direct (Supplementary Table 3).

As a complimentary analysis, we used Alphapulldown to evaluate all 279 identified PPI partners. Of these, 32 interactions (11.5%) were predicted *in silico* to be direct, including HNRNPU multimerization, which has been described earlier (1) (Supplementary Table 4). The most significant proteins predicted to interact directly with HNRNPU were DEAD-box helicases DDX17 and DDX5, which we also identified at D0 (Supplementary Table 3).

Among the identified interacting partners at D0, we performed GO enrichment analysis and identified the following six protein network hubs with significant enrichment: cytoplasmic translation (FDR $2.4x10^{-103}$), negative regulation of translation (FDR $1.9x10^{-11}$), RNA splicing (FDR $9.2x10^{-79}$), actin cytoskeleton reorganization (FDR $1.2x10^{-3}$), negative regulation of proteolysis (FDR $1.6x10^{-4}$) and mammalian SWI-SNF (mSWI/SNF, also known as BAF) complex proteins (FDR $3.4x10^{-19}$) (Figure 1B). For D28 proteins, three of these networks were present and significant (Supplementary Figure S1B). Interestingly, none of the mSWI-SNF complex

network proteins were earlier indicated as interacting partners of HNRNPU in the BioGRID database.

The GSEA of GO terms for all HNRNPU-interacting proteins was in line with identified networks, with highly significant terms related to cytoplasmic translation (FDR $4.4x10^{-87}$ and $3.88x10^{-29}$ at D0 and D28, respectively), mRNA stabilization ($6.62x10^{-5}$ and $1.65x10^{-6}$) and RNA splicing ($1.26x10^{-10}$ at D0) (Figure 1C, Supplementary Figure S1C, Supplementary Table 5). Furthermore, cell type enrichment analysis using EWCE of neural cell types at mid-gestation (44) revealed that HNRNPU-interacting proteins are enriched in progenitor cells with high HNRNPU expression (Figure 1D, Supplementary Figure S1D-E, Supplementary Table 6). No statistically significant enrichment was detected for ASD, ID, or epilepsy gene lists among the PPI partners despite many of the proteins being encoded by causative NDD genes such as the mSWI-SNF complex (47), PUM1 (48) and ATAD3 (49) (Supplementary Figure S1F, Supplementary Table 7).

We validated four direct PPIs (FUS, EEF2, NUFIP2, and DDX17) and one RNA-assisted PPI (ARID1B) at D0 with PLA (Figure 1E). We found that HNRNPU-EEF2 interaction occurs in the cytoplasm despite the predominant nuclear localization of the HNRNPU protein (Figure 1E). We confirmed the presence of HNRNPU in the cytoplasm using super-resolution microscopy (Supplementary Figure S1G) and found that the cytoplasmic HNRNPU fraction increases at D7 and decreases by D14, whereas the nuclear fraction decreases in concordance with the whole fraction and our earlier RNA-Seq data (10) (Supplementary Figure S1H, Supplementary Figure S5).

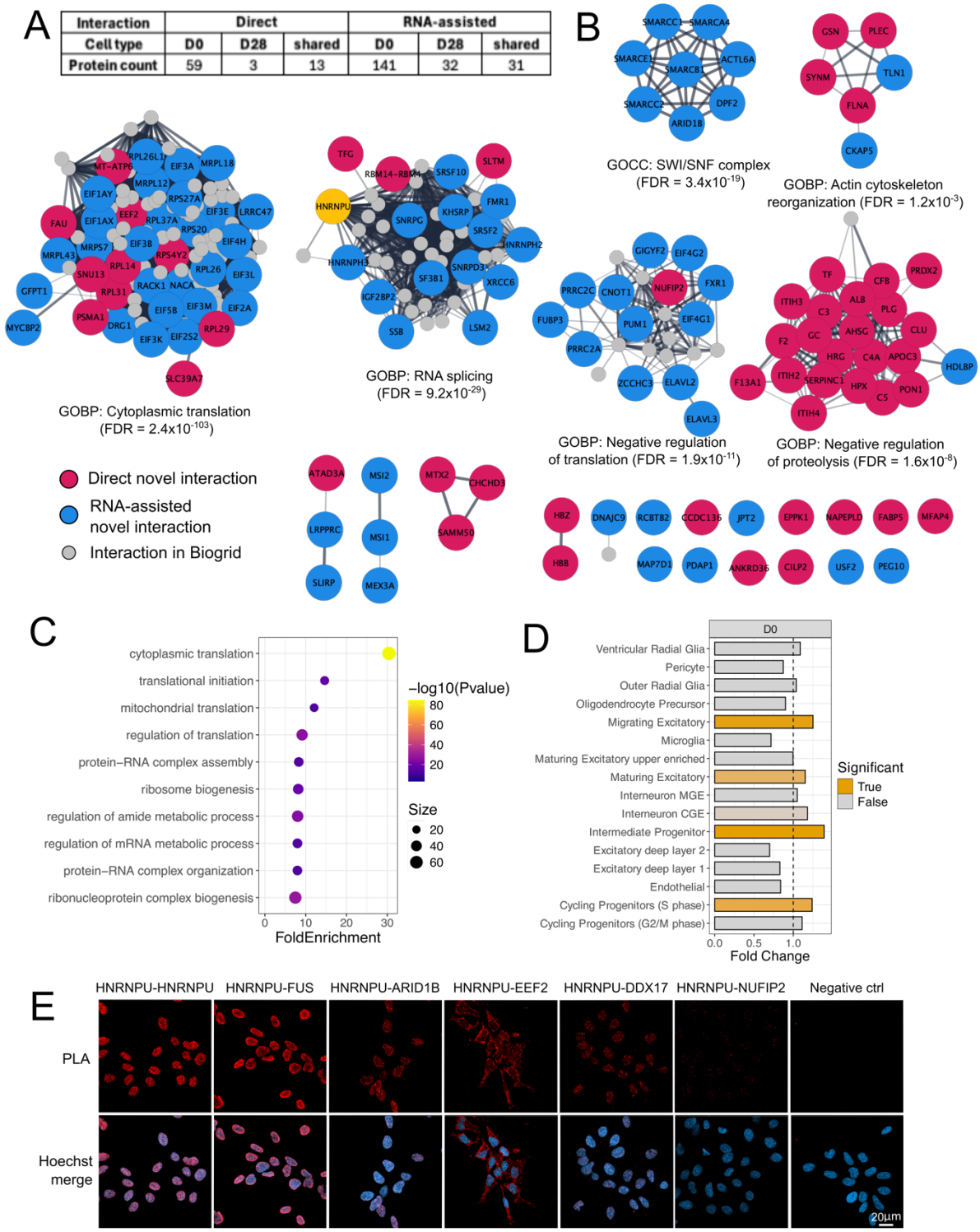

Figure 1: Identification and characterization of HNRNPU protein-protein interaction networks in neural cells. A) Number of identified PPI partners of HNRNPU at D0 and D28 based on IP-MS experiments. B) Interactome map based on STRING database analysis of identified proteins interacting with HNRNPU at D0. The red and blue nodes represent whether the interaction was

novel and classified as direct or RNA-assisted based on RNase A-treated samples, whereas grey nodes represent proteins with already identified interactions with HNRNPU. The most significantly enriched GO biological process (GOBP) or GO cellular component (GOCC) is shown for each identified network C) GO biological process enrichment analysis from all HNRNPU interacting proteins at D0, after merging direct and RNA-assisted interactions. D) Cell type enrichment analysis of all PPI partners identified at D0 into fetal brain mid-gestation scRNA-Seq data. E) Proximity Ligation Assay (PLA) panel representing HNRNPU interaction with the selected interacting partners. HNRNPU-HNRNPU samples were incubated with two different anti-HNRNPU antibodies. Negative control represents cells incubated without primary antibodies. Scale bar, 20 μm.

HNRNPU binds mRNAs encoding proteins related to RNA processing and neuronal development

Next, we sought to identify RNA targets of HNRNPU using fRIP-Seq at D0 and D28. We identified 22123 and 11197 significant peaks using CLAM peak calling software (50), annotated to 2029 and 913 individual genes for D0 and D28, respectively (Supplementary Table 8). Of these, 448 genes shared hits across both time points. The majority of the targets were protein-coding mRNAs (86.0% and 77.2% for D0 and D28, respectively) and long non-coding RNAs (9.2% and 12.5%), whereas the fraction of snoRNA increased from D0 (1.3%) to D28 (3.7%) (Figure 2A). The HNRNPU RNA-binding motif (UGUAUUG) was detected in 92.8% and 91.6% of the mRNA peak region sequences at D0 and D28, respectively, although the enrichment was not significant (FDR 0.849 and 0.806 at D0 and D28, respectively) (Supplementary Table 9). We compared our data to published fRIP-Seq (23) and CLIP-Seq datasets (42) from non-neural cell types and identified 1.7% and 29% overlap between target genes, respectively (Figure 2B).

Many HNRNPU targets were enriched in GO-BP terms, such as cytoplasmic translation (FDR $7.2x10^{-43}$) and mRNA metabolic processes (FDR $7.5x10^{-16}$) at D0 and neurodevelopmental processes such as neurite (FDR $2.2x10^{-18}$) and axon development (FDR $7.0x10^{-11}$) at D28 (Figure 2C, Supplementary Table 5). Furthermore, we found a significant enrichment between HNRNPU-bound RNAs and gene lists associated with ASD (FDR $1.0x10^{-5}$ and $4.3x10^{-10}$ for D0 and D28, respectively), ID (FDR $3.7x10^{-11}$ and $2.0x10^{-9}$) and epilepsy (FDR $9.4x10^{-4}$ and $2.5x10^{-5}$) (hypergeometric test, Figure 2D, Supplementary Table 7). Furthermore, while shared

enrichments for cell types for HNRNPU targets were identified at D0 and D28, we also found specific enrichments at each timepoint (Figure 2E, Supplementary Table 6). For instance, D0 targets were enriched in progenitors and ventricular radial glia cells, while D28 targets were enriched in interneurons from medial ganglionic eminence (MGE), upper enriched maturing excitatory neurons, and deep layer 1 excitatory neurons.

To identify RNA targets that could be shared targets of the HNRNPU PPI partners, we compiled a list of RNA motifs, including motifs for 132 RBPs (Supplementary Table 1), out of which 31 proteins were also pulled down in our MS-IP experiment. We identified 29 and 10 proteins having significant motif enrichment in our fRIP-seq data at D0 and D28, respectively (Supplementary Table 10). Of these, six proteins at D0 (SRSF10, HNRNPH2, IGF2BP3, EWSR1, FUS, and FUBP3), and two proteins at D28 (HNRNPH2 and YBX1) were pulled down together with HNRNPU in our IP-MS. Four of these were identified as RNA-assisted PPIs, and three (EWSR1, FUS, and YBX1) were direct HNRNPU-interacting proteins (Supplementary Table 3).

Next, we assessed whether HNRNPU targets are differentially abundant (DA) or spliced (DS) in HNRNPU deficiency state by comparing them with available RNA-Seq data from HNRNPU-deficient human 2D and 3D models and mouse models reported previously (10, 11, 13). Overall, the overlap between HNRNPU binding and simultaneous DA or DS was low, which is in line with earlier work (4, 9) (Supplementary Figure S2A, Supplementary Table 8). Twenty-seven targets were DA on all datasets, including *NTRK2*, *DCX*, *NEUROD1,* and *ROBO3* mRNAs. Furthermore, comparing only to our 2D model RNA-seq at D0, D5, and D28 DA mRNAs, we found several neurodevelopmentally relevant targets to be simultaneously bound by HNRNPU and downregulated in relation to HNRNPU deficiency, such as *PAX3* and *PLXNA2* mRNAs at D0 as well as *RORB*, *NEUROD1* and *ROBO3* mRNAs at D28. On the contrary, *LIN28A* and *PRTG* mRNAs at D0 and *CDK6*, *SOX11* and *NES* mRNAs at D28 were upregulated and bound by HNRNPU. Out of 315 DA mRNAs, 60 and 68 were also DA in *HNRNPU*-mutant 3D and mouse models, respectively (Supplementary Table 8). Similarly, in our 2D model, several bound and DS targets at D28 included mRNAs encoding proteins with critical neurodevelopmental functions, including *ANK2*, *ANK3*, *DCLK1*, *GPC1* and *NCAM1* mRNAs. Furthermore, out of 153 bound and DS targets, 33 were also DS in the mouse model, such as *NRXN1* and *RMST* mRNAs (Supplementary Table 8).

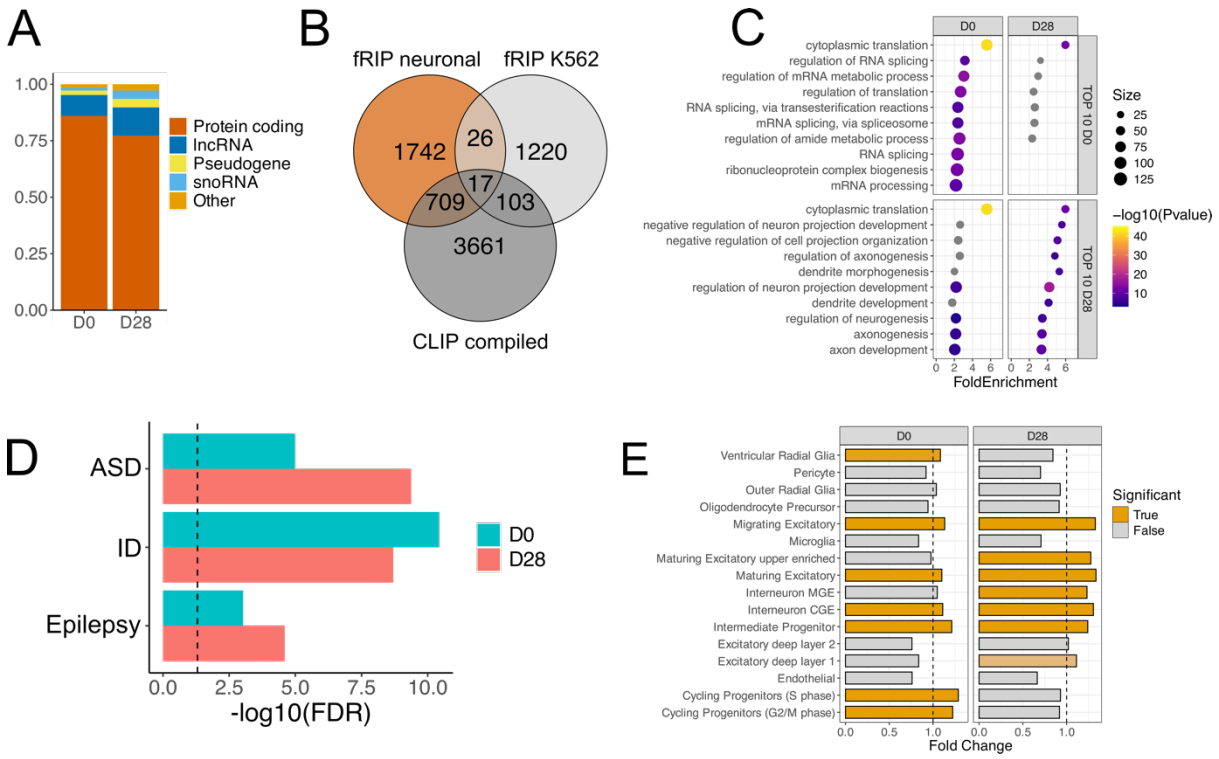

Figure 2: HNRNPU RNA targets and their enrichment in neurodevelopmental processes. A) Fraction of HNRNPU target RNA biotypes at D0 and D28. Biotype "Other" represents miRNA, snRNA, sRNA, ribozyme and misc_RNA. B) Overlap of HNRNPU targets from our fRIP-Seq datasets at D0 and D28 (fRIP neuronal) and published fRIP-Seq dataset on K562 cells (23) (fRIP K562) and eCLIP/HITS-CLIP datasets from HeLa, K562, and HepG2, as well as human adrenal gland tissue (CLIP). C) GO biological process enrichment analysis on HNRNPU target RNAs at D0 and D28. Represented are the top 10 significant terms from each time point. D) Enrichment of the host genes of HNRNPU target RNAs at D0 and D28 in autism (ASD), intellectual disability (ID) and epilepsy risk gene lists. The vertical dotted line represents the significance threshold of FDR<0.05 (-log10(FDR)>1.3) after hypergeometric analysis. E) Cell type enrichment analysis of HNRNPU target RNAs at D0 and D28 into fetal mid-gestation scRNA-Seq data.

Functional impacts of HNRNPU on mRNA stability and translation of selected targets

Next, we aimed to investigate the effect of HNRNPU binding to those mRNAs highly enriched in the fRIP-Seq data (Figure 3A, Supplementary Table 11) that encode proteins with known relevance to neuronal development and were neither differentially spliced nor differentially abundant in HNRNPU deficiency in our published RNA-Seq data, namely *TRIM2*, *KLF12*, *ERBB4, CDK6* and *TNPO1* mRNAs. We also included *QSER1* mRNA, which has no known connection to neuronal development but was the second most significant target of HNRNPU and was

recently shown to protect bivalent promoters from hypermethylation by cooperating with TET1 (51). We confirmed that silencing HNRNPU did not affect the levels of *TRIM2*, *KLF12*, or *ERBB4* mRNAs, but significantly increased the levels of *TNPO1* and CDK6 mRNAs, and non-significantly increased *QSER1* mRNA (Figure 3B Supplementary Figure S3A). HNRNPU silencing stabilized *TRIM2*, *QSER1* and *ERBB4* mRNA, slightly modified *KLF12* mRNA stability and had no effect on the stabilities of *TNPO1* or *CDK6* mRNAs nor that of *NPM1* mRNA, which is not an HNRNPU target (Figure 3C, Supplementary S3B). We, furthermore, tested the HNRNPU depletion effect on QSER1 protein levels and observed a nonsignificant upregulation at D0 (p-value=0.52) and D7 (p-value=0.16) (Figure 3D).

Given the validated cytoplasmic localization of HNRNPU and the enrichment of its PPI partners and target mRNAs in translation-related processes, we next investigated if HNRNPU has a global role in mRNA translation. For this, we fractionated polysomes and studied if the relative size of polysomes forming on target mRNAs differed after modulating HNRNPU levels. The overall distribution of polysomes did not appear to vary significantly except for a slight increase in the 80S peak when HNRNPU was downregulated (Figure 3E). Polysome profiling followed by western blot analysis revealed the presence of HNRNPU in fractions one to four (corresponding to soluble fractions), and in the 40S (small ribosomal subunit), 60S (large ribosomal subunit), and 80S (monosome) fractions (Supplementary Figure S3C). Since the overall abundance of *TNPO1*, *CDK6,* and *QSER1* mRNAs increased, they were excluded from RT-qPCR analysis in polysomes.

Interestingly, the distribution of *ERBB4* mRNA across the sucrose gradients (Figure 3F) showed a shift away from the higher translating polysomes (fractions 10-12) toward lower-molecular-weight polysomes (fractions 7-9), suggesting a potential role for HNRNPU in the translation of *ERBB4* mRNA. Furthermore, we observed similar polysome distributions for *TRIM2* and *KLF12* mRNAs: both displayed slightly elevated percentages of mRNA in fraction 4 (80S peak) and fractions 7-9 (low molecular weight polysomes) in the siHNRNPU samples (Supplementary Figure S3D). However, the distribution curve of non-target *NPM1* mRNA shared these same attributes (Figure 3F), suggesting these slight changes may be due to experimental conditions and do not reflect HNRNPU-specific changes.

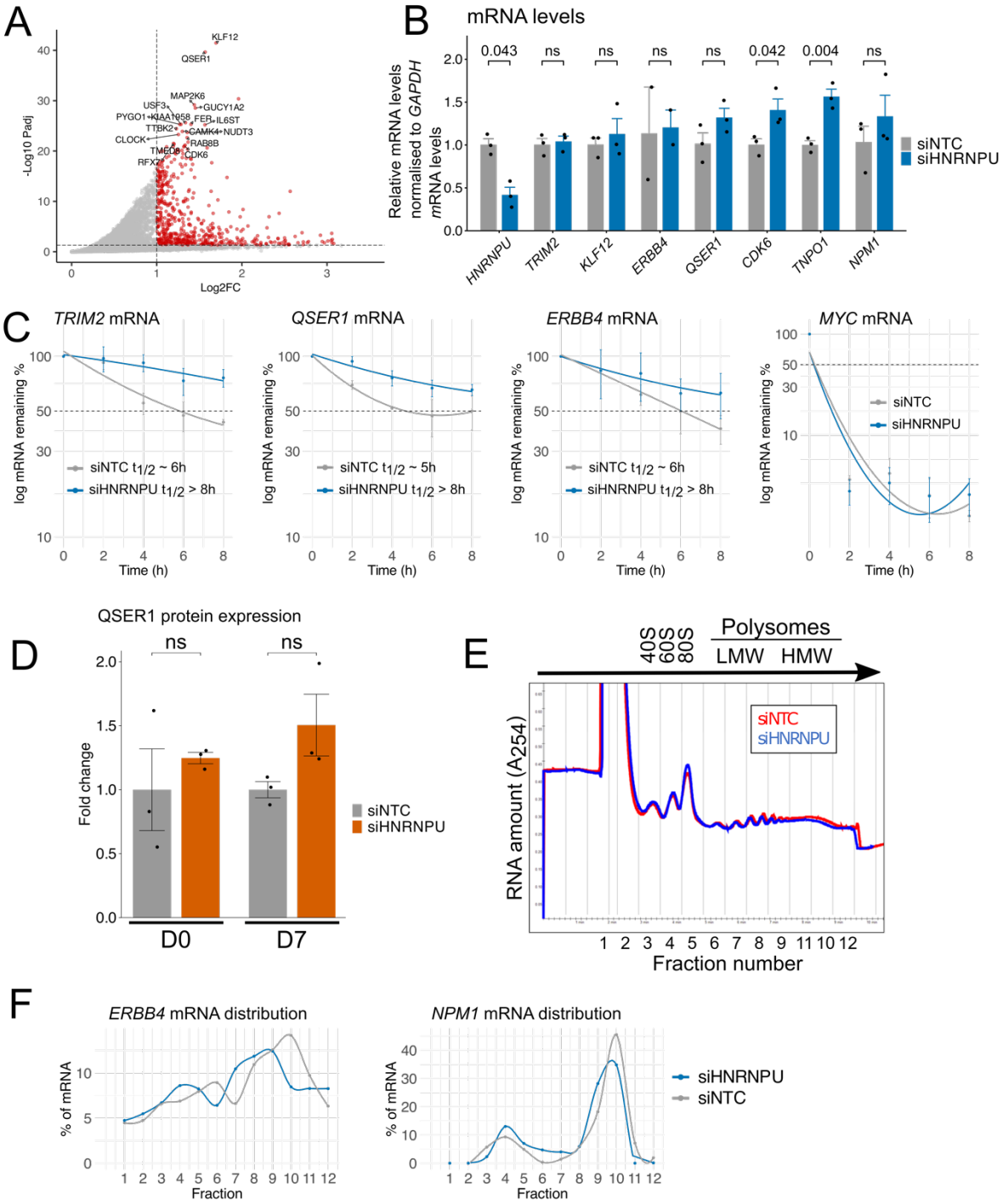

Figure 3: Impact of HNRNPU silencing on mRNA stability and translation in neural cells. A) A volcano plot representing DESeq2 enrichment analysis on fRIP-Seq data to identify the most abundantly enriched RNA targets of HNRNPU at D0. B) RT-qPCR analysis of the levels of *HNRNPU* mRNA, the HNRNPU targets *TRIM2*, *KLF12*, *ERBB4*, *QSER1*, *CDK6* and *TNPO1* mRNAs, as well as a non-target *NPM1* mRNA at D0 after HNRNPU silencing (n=2 or 3). Expression levels were normalized to the levels of *GAPDH* mRNA. Error bars represent standard error of the mean (SEM). C) RT-qPCR analysis of the stability of HNRNPU targets *TRIM2*, *QSER1* and

ERBB4 mRNA as well as a labile control *MYC* mRNA at D0 cells after HNRNPU silencing and actinomycin D treatment for the indicated times. The levels of target mRNAs were normalized to the levels of *GAPDH* mRNA. Error bars represent SEM. D) Quantification of QSER1 protein expression after HNRNPU downregulation, measured by JESS capillary western blot analysis, using total protein for normalization. Represented are fold changes relative to siNTC samples. Significance was calculated using Student's t-test (n=3). E) Cytoplasmic lysates after HNRNPU downregulation were fractionated through sucrose gradients to evaluate polysome profiles. Fractions 1-2 represent fractions without ribosomal material, 3-5 correspond to 40S, 60S, 80S monosomes, 7-9 correspond to low-molecular-weight polysomes (LMW) and 10-12 to high-molecular-weight polysomes (HMW). F) The relative distribution of HNRNPU target *ERBB4* mRNA and a non-target *NPM1* mRNA across the fractionated polysome gradients was calculated by RT-qPCR analysis (n=1).

A complex network of HNRNPU interaction with mSWI-SNF complex and regulation of DNA methylation regulators affects the methylation state of NES cells

Given that recent studies have reported a distinct methylation signature in blood samples from individuals with HNRNPU-related NDDs (20, 21), and our results show that *QSER1*, *TET1* and *TET3* mRNAs are RNA targets of HNRNPU (Figure 4A, Supplementary Figure S4A), we sought to investigate the dynamic regulatory patterns of DNA methylation factors and the mSWI/SNF complex in our cell model. The longitudinal gene expression profiling in our cell system indicated four distinct expression group profiles (Figure 4B). For instance, we found that HNRNPU targets *QSER1*, *TET1* and *SMARCC2* mRNAs, the latter encoding a protein that is an HNRNPU PPI partner, together with non-target *DNMT3A* mRNA have low expression levels at D0 followed by an increase at D5, when the neurogenesis is occurring, and decrease again by D28. In contrast, *TET3*, *ARID1B* and *SMARCA4* mRNAs gradually increase throughout differentiation.

We, thus, hypothesized that global 5-methylcytosine (5mC) levels would be altered in the HNRNPU-deficient state at D0 but also at D7, potentially linked to the differences in the expression of demethylation enzymes. Indeed, HNRNPU silencing significantly decreased global 5mC level at D0 (p-value=0.029) and led to a non-significant decrease at D7 (p-value=0.061) (Figure 4C, Supplementary Figure S4B). Analysis of TET1/2/3 and DNMT1/3A/3B protein levels upon HNRNPU silencing revealed a significant upregulation of TET3 260 and 110

kDa protein isoforms (p-value 0.043 and 0.018, respectively) and DNMT3A2 (p-value 0.046) at D7 (Figure 4D). No differences were observed for TET1/2 or DNMT3A/B isoforms (Supplementary Figure S4C-I). Based on these findings, we conclude that the role of HNRNPU in chromatin regulation, putatively through its interactions with the mSWI/SNF complex, is more crucial for the global methylation pattern than regulating the demethylation enzymes.

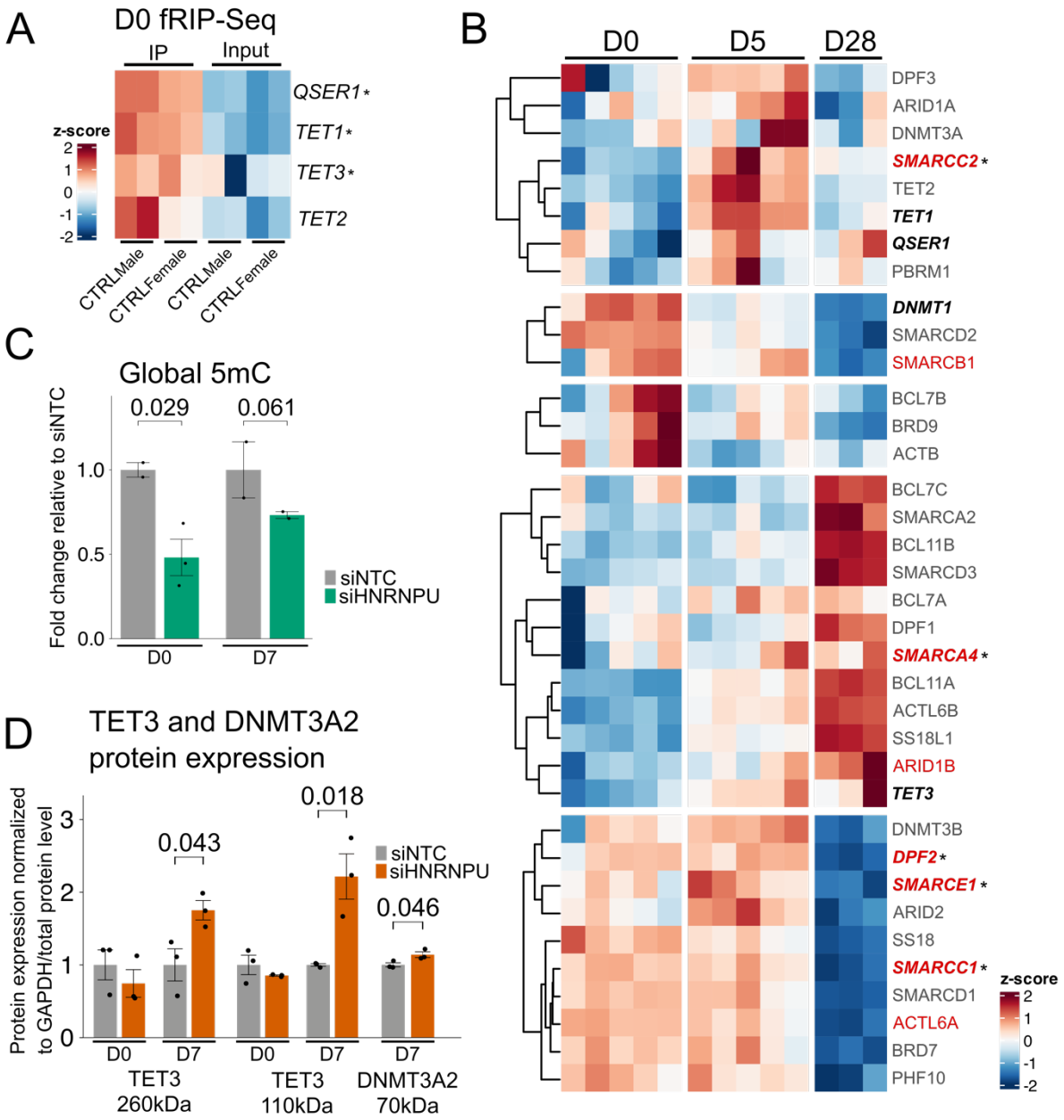

Figure 4: Role of HNRNPU in regulating DNA methylation and epigenetic dynamics in neural differentiation. A) Heatmap highlighting the expression levels of *QSER1*, *TET1*, *TET3* and *TET2* mRNAs from fRIP-Seq data at D0. Asterisks represent significant HNRNPU targets. B) Heatmap of expression dynamics of the mRNAs encoding mSWI/SNF complex subunits, DNA

methyltransferases (DNMT1, DNMT3A/B), TET enzymes (TET1/2/3) and QSER1 in our published RNA-Seq dataset on $CTRL_{Male}$ cell line across differentiation time points D0, D5 and D28. The gene names are in red if the protein was a significant HNRNPU PPI partner in our MS-IP, in italics bold if mRNA was a significant HNRNPU target, or in red and italics bold together with an asterisk if the target was significant in both datasets. Genes in grey are relevant for mSWI-SNF complex/DNA methylation regulation but showed no significant enrichment in our IP-MS or fRIP-Seq datasets. C) Global 5mC levels in DNA after HNRNPU downregulation at D0 and D7. The data are represented as a fold change relative to control samples. D) Western blot quantification of TET3 260 and 110 kDa isoforms after HNRNPU silencing. Data were normalized to GAPDH protein level and represented as a fold change relative to siNTC samples. Error bars represent SEM, and statistical significance was calculated using Student's t-test (n=3).

DISCUSSION

Our study provides a comprehensive analysis of the molecular roles of HNRNPU, an important NDD gene, in NES and differentiating neural cells, highlighting its impact on processes affecting gene expression, including mRNA translation, chromatin remodelling complexes, and DNA methylation regulators. Many of the found PPI partners and RNA targets were novel or not described in detail in earlier literature, highlighting the need for cell type- and state-specific interactome analysis (52, 53).

Earlier studies have focused on transcriptomic changes associated with HNRNPU deficiency. However, the direct targets of HNRNPU in RNA regulation and the initial effects of HNRNPU downregulation remained unexplored. Here, we showcase that the direct RNA targets of HNRNPU encode proteins important for neuronal development and are associated with ASD, ID, and epilepsy. Furthermore, we identified key targets that were directly bound by HNRNPU and also differentially abundant or spliced in human 2D and 3D cultured cell models as well as in a mouse in vivo knockout model. For instance, *DCX* mRNA, encoding a protein crucial for cortical neuronal migration (54, 55), was a common differentially expressed HNRNPU target across brain development models, and its dysregulation could relate to severe cortex development defects seen in *Hnrnpu* knockout mice (13). Similarly, we identified *ROBO3* and *NEUROD1* mRNAs as HNRNPU targets with consistently dysregulated abundance across

all HNRNPU deficiency models, further underscoring the critical role of HNRNPU in neuronal development. *ROBO3* mRNA encodes a member of the ROBO receptor family that has been shown to play a key role in cortical interneuron development (56).

Given the high enrichment of translation-related proteins in our IP-MS, the verified cytoplasmic localization, and recent evidence of HNRNPU regulating translation of target mRNAs in relation to cancer (57), we investigated the effects of HNRNPU downregulation on neural target mRNAs. We found that while global translation seemed to be unaffected, HNRNPU can regulate the translation of specific mRNAs, similar to what has been shown to other RBPs such as LIN28A (58) and HNRNPC (59). One such target was *ERBB4* mRNA, encoding the tyrosine-protein kinase ERBB4 that plays a role in the central nervous system and heart development and is also associated with NDDs (60). It was noteworthy that the processes related to translation were significant both for the PPI partners and RNA targets of HNRNPU. This observation could indicate a robust regulatory loop to control the translation machinery and the levels of protein synthesis. Moreover, the downregulation of ribosomal proteins was reported as one of the most prominent biological processes downregulated in HNRNPU mutant human cortical organoids (11). To date, there have not been any proteomic-wide studies done in HNRNPU models, so further studies should provide a more comprehensive evaluation of the effects using high-throughput methods such as translatome analyses (61).

Finally, our findings support the role of HNRNPU in regulating chromatin accessibility and DNA methylation during neural differentiation, likely in cooperation with the mSWI/SNF complex. For instance, HNRNPU binds both *SMARCC1* and *SMARCC2* mRNAs and then interacts with the encoded proteins, suggesting that HNRNPU plays a multifaceted role in controlling the important transitions across neural development. Earlier evidence has shown that SMARCC1 (BAF155) is involved in the transition from neural progenitors to differentiated neurons with interacting transcription factors like PAX6 to regulate cortical development and progenitor cell division (62). On the other hand, SMARCC2 (BAF170) is shown to be needed for the maturation of neural cells (63). Considering earlier evidence of HNRNPU localizing near transcription start sites and active promoters (1–3), we propose that HNRNPU, together with mSWI/SNF complex, facilitates access for transcription factors, DNMTs, and TET enzymes to specific DNA regions dynamically throughout early neuronal development to ensure correct transitions and differentiation patterns (64, 65). Moreover, a recent study also detected

interactions between HNRNPU and mSWI/SNF proteins in pluripotent stem cells (25), suggesting this interplay may play roles beyond neuronal development.

However, our results reveal inconsistencies that suggest a more complex regulatory mechanism. While TET3 protein levels were increased significantly at D7, global 5mC levels were lower without reaching significance. This could indicate that compensatory mechanisms counteract the initial hypomethylation seen upon HNRNPU silencing at D0 or that DNA methylation changes are localized to specific sites rather than occurring globally. Additionally, DNMT3A2 upregulation at D7, despite not being an HNRNPU target, suggests indirect regulation, possibly through chromatin changes or interactions with other transcriptional regulators. Based on our results we can speculate about the exact mechanisms in which HNRNPU deficiency contributes to DNA methylation regulation at D0 being a neural epithelial stem cell stage. As one putative model, we suggest that chromatin compaction following *HNRNPU* silencing (2, 10) prevents key regulators like DNMT1 from accessing their target DNA. A similar inability of DNMT1 to bind DNA has been linked to global DNA hypomethylation (66), resembling our findings after *HNRNPU* silencing. Loss of DNMT1 catalytic activity has also been associated with proliferative neural progenitors (67) and retinal neuronal progenitors that either fail to exit the cell cycle or experience disruptions in early neuronal maturation (68), aligning with the increased proliferation and delayed differentiation seen in our *HNRNPU*-deficient in vitro model (10). Moreover, we found that HNRNPU binds to *TET3* and *QSER1* and alters the protein levels encoded by these mRNAs, suggesting another layer by which HNRNPU may regulate DNA methylation which we only observed at the stage of neural progenitor stage of our model (D5-D7). Notably, *QSER1-TET1* double knockout in human embryonic stem cells disrupted the differentiation into pancreatic progenitors (51). The highly similar phenotypes in the clinical syndromes caused by the mSWI/SNF complex genes, Coffin-Siris syndrome (47) and TET3, Beck-Fahrner syndrome (69), and the HNRNPU-related NDDs further strengthen our hypothesis.

As a second hypothetical model, based on a novel function of HNRNPU in degrading RNA in m6A-dependent fashion via METTL3-METTL14/YTHDF2 axis (70), we speculate that HNRNPU may influence DNA methylation through m6A-modified RNAs. Since m6A modifications in chromatin-associated RNAs affect chromatin organization (71), and m6A depletion increases 5mC levels without altering TET1/2/3 or DNMT1/3A/3B expression (72), this is a mechanism that should be further studied. Interestingly, another HNRNP protein,

HNRNPC, has selective affinity to bind m6A-remodeled RNA structures (73). All this evidence and putative mechanisms underscores the need for further research to understand how HNRNPU influences epigenetic switches during developmental phases, which could explain the multifaceted and systematic developmental phenotypes seen in individuals with HNRNPU-related NDDs.

Despite having found many novel roles and strengthened the earlier described roles of HNRNPU, we acknowledge several limitations. The HNRNPU protein is highly expressed in neural stem cells at D0, making it challenging to silence it efficiently. A challenge that is not only seen in oligo-based silencing approaches as the expression has been shown to be variable even with genome-engineered loss-of-function mutations (11). We also acknowledge that the 2D cell model used in this study is not a comprehensive representation of human brain development, and more work is needed to understand the dynamic regulation of HNRNPU in more complex 3D brain development models.

In conclusion, we present a comprehensive mapping of the HNRNPU molecular interactome in neural cells. Our study highlights the critical role of HNRNPU in neuronal development through its interactions with RNA regulatory pathways, including regulating translation, chromatin remodeling complexes, and DNA methylation regulators. Follow-up studies of both protein expression and DNA methylation changes associated with HNRNPU-related NDDs will be needed to better assess the role of HNRNPU in neural development and pathogenesis of *HNRNPU*-related NDDs.

ACKNOWLEDGEMENTS

The data handling was enabled by resources in project NAISS provided by the National Academic Infrastructure for Supercomputing in Sweden (NAISS) at UPPMAX, funded by the Swedish Research Council through grant agreement no. 2022-06725. We thank the PDC Center for High Performance Computing, KTH Royal Institute of Technology, Sweden, for providing access to the computing resources used in this research. We also would like to thank the core facility at NEO, BEA, Bioinformatics and Expression Analysis, which is supported by the board of research at the Karolinska Institute and the research committee at the Karolinska hospital.

Mass spectrometry analysis was performed by the Clinical Proteomics Mass Spectrometry facility, Karolinska Institutet/ Karolinska University Hospital/ Science for Life Laboratory.

AUTHOR CONTRIBUTIONS

Conceptualization: M.O., F.M., K.M.M., M.G., and K.T.; Methodology and Data Analysis: M.O., F.M., K.M.M, J.M., X.Y., A.A., N.B., M.G., and K.T.; Validation: M.O., F.M., and K.T.; Resources: M.G. and K.T.; Data Curation: M.O., F.M,; Writing – Original Draft: M.O., and K.T.; Writing – Review & Editing: M.O., and K.T.; Visualization: M.O., and K.T.; Supervision: M.G., and K.T.; Project Administration: M.O., F.M., K.M.M., M.G., and K.T.; Funding Acquisition: M.O, K.T, Critical review of the draft: All authors.

SUPPLEMENTARY DATA

Supplementary Data are available at NAR online.

CONFLICT OF INTEREST

The authors have no conflicts to declare.

FUNDING

This work was supported by grants from the Swedish Research Council [2017-01660 to K.T., 2023-02111 to K.T.]; Swedish Foundation for Strategic Research [FFL18-0104 to K.T.]; the Swedish Brain Foundation – Hjärnfonden [to K.T.].; KI-NIH PhD program for PhD students [M.O.]; Osk. Huttunen Foundation [to M.O.]; the H.K.H. Kronprinsessan Lovisas förening för barnasjukvård och Stiftelsen Axel Tielmans minnesfond [2020-00573 to F.M., 2021-00617 to F.M., 2023-00784 to M.O., 2024-032 to M.O.]; the Strategic Research Area Neuroscience (StratNeuro) at Karolinska Institutet [to K.T.]; KI Foundations [to K.T.]; the Committee for Research at Karolinska Institutet [to K.T.]., Funding for open access charge: Karolinska Institute: Karolinska Institutet. K.M.M., J.L.M., N.B., and M.G. were supported by the NIA IRP, NIH.

DATA AVAILABILITY

All Raw and/or processed data will be available in suitable repositories upon publication.

REFERENCES

1. Nozawa,R.S., Boteva,L., Soares,D.C., Naughton,C., Dun,A.R., Buckle,A., Ramsahoye,B., Bruton,P.C., Saleeb,R.S., Arnedo,M., *et al.* (2017) SAF-A Regulates Interphase Chromosome Structure through Oligomerization with Chromatin-Associated RNAs. *Cell*, 169, 1214-1227.e18.
2. Fan,H., Lv,P., Huo,X., Wu,J., Wang,Q., Cheng,L., Liu,Y., Tang,Q.Q., Zhang,L., Zhang,F., *et al.* (2018) The nuclear matrix protein HNRNPU maintains 3D genome architecture globally in mouse hepatocytes. *Genome Res*, 28, 192–202.
3. Han,B. yue, Liu,Z., Hu,X. and Ling,H. (2022) HNRNPU promotes the progression of triple-negative breast cancer via RNA transcription and alternative splicing mechanisms. *Cell Death Dis*, 13.
4. Huelga,S.C., Vu,A.Q., Arnold,J.D., Liang,T.D., Liu,P.P., Yan,B.Y., Donohue,J.P., Shiue,L., Hoon,S., Brenner,S., *et al.* (2012) Integrative Genome-wide Analysis Reveals Cooperative Regulation of Alternative Splicing by hnRNP Proteins. *Cell Rep*, 1, 167–178.
5. Ye,J., Beetz,N., O'Keeffe,S., Tapia,J.C., Macpherson,L., Chen,W. V., Bassel-Duby,R., Olson,E.N. and Maniatis,T. (2015) HnRNP U protein is required for normal pre-mRNA splicing and postnatal heart development and function. *Proc Natl Acad Sci U S A*, 112, E3020–E3029.
6. Yugami,M., Kabe,Y., Yamaguchi,Y., Wada,T. and Handa,H. (2007) hnRNP-U enhances the expression of specific genes by stabilizing mRNA. *FEBS Lett*, 581, 1–7.
7. Zhao,W., Wang,L., Zhang,M., Wang,P., Qi,J., Zhang,L. and Gao,C. (2012) Nuclear to Cytoplasmic Translocation of Heterogeneous Nuclear Ribonucleoprotein U Enhances TLR-Induced Proinflammatory Cytokine Production by Stabilizing mRNAs in Macrophages. *The Journal of Immunology*, 188, 3179–3187.
8. Gañez-Zapater,A., Mackowiak,S.D., Guo,Y., Tarbier,M., Jordán-Pla,A., Friedländer,M.R., Visa,N. and Östlund Farrants,A.K. (2022) The SWI/SNF subunit BRG1 affects alternative splicing by changing RNA binding factor interactions with nascent RNA. *Molecular Genetics and Genomics*, 297, 463–484.
9. Xiao,R., Tang,P., Yang,B., Huang,J., Zhou,Y., Shao,C., Li,H., Sun,H., Zhang,Y. and Fu,X.D. (2012) Nuclear Matrix Factor hnRNP U/SAF-A Exerts a Global Control of Alternative Splicing by Regulating U2 snRNP Maturation. *Mol Cell*, 45, 656–668.
10. Mastropasqua,F., Oksanen,M., Soldini,C., Alatar,S., Arora,A., Ballarino,R., Molinari,M., Agostini,F., Poulet,A., Watts,M., *et al.* (2023) Deficiency of the Heterogeneous Nuclear Ribonucleoprotein U locus leads to delayed hindbrain neurogenesis. *Biol Open*, 12.

11. Ressler,A.K., Sampaio,G.L.A., Dugger,S.A., Sapir,T., Krizay,D., Boland,M.J., Reiner,O. and Goldstein,D.B. (2023) Evidence of shared transcriptomic dysregulation of HNRNPU-related disorder between human organoids and embryonic mice. *iScience*, 26.
12. Dugger,S.A., Dhindsa,R.S., Sampaio,G.D.A., Ressler,A.K., Rafikian,E.E., Petri,S., Letts,V.A., Teoh,J.J., Ye,J., Colombo,S., *et al.* (2023) Neurodevelopmental deficits and cell-type-specific transcriptomic perturbations in a mouse model of HNRNPU haploinsufficiency. *PLoS Genet*, 19.
13. Sapir,T., Kshirsagar,A., Gorelik,A., Olender,T., Porat,Z., Scheffer,I.E., Goldstein,D.B., Devinsky,O. and Reiner,O. (2022) Heterogeneous nuclear ribonucleoprotein U (HNRNPU) safeguards the developing mouse cortex. *Nat Commun*, 13, 4209.
14. Kanai,Y., Dohmae,N. and Hirokawa,N. (2004) Kinesin Transports RNA: Isolation and Characterization of an RNA-Transporting Granule.
15. Kipper,K., Mansour,A. and Pulk,A. (2022) Neuronal RNA granules are ribosome complexes stalled at the pre-translocation state. *J Mol Biol*, 434.
16. Depienne,C., Nava,C., Keren,B., Heide,S., Rastetter,A., Passemard,S., Chantot-Bastaraud,S., Moutard,M.L., Agrawal,P.B., VanNoy,G., *et al.* (2017) Genetic and phenotypic dissection of 1q43q44 microdeletion syndrome and neurodevelopmental phenotypes associated with mutations in ZBTB18 and HNRNPU. *Hum Genet*, 136, 463–479.
17. Taylor,J., Spiller,M., Ranguin,K., Vitobello,A., Philippe,C., Bruel,A.L., Cappuccio,G., Brunetti-Pierri,N., Willems,M., Isidor,B., *et al.* (2022) Expanding the phenotype of HNRNPU-related neurodevelopmental disorder with emphasis on seizure phenotype and review of literature. *Am J Med Genet A*, 10.1002/ajmg.a.62677.
18. Sapir,T. and Reiner,O. (2023) HNRNPU's multi-tasking is essential for proper cortical development. *BioEssays*, 45.
19. Gillentine,M.A., Wang,T., Hoekzema,K., Rosenfeld,J., Liu,P., Guo,H., Kim,C.N., De Vries,B.B.A., Vissers,L.E.L.M., Nordenskjold,M., *et al.* (2021) Rare deleterious mutations of HNRNP genes result in shared neurodevelopmental disorders. *Genome Med*, 13, 63.
20. Rooney,K., van der Laan,L., Trajkova,S., Haghshenas,S., Relator,R., Lauffer,P., Vos,N., Levy,M.A., Brunetti-Pierri,N., Terrone,G., *et al.* (2023) DNA methylation episignature and comparative epigenomic profiling of HNRNPU-related neurodevelopmental disorder. *Genetics in Medicine*, 25.
21. Lee,S., Ochoa,E., Badura-Stronka,M., Donnelly,D., Lederer,D., Lynch,S.A., Gardham,A., Morton,J., Stewart,H., Docquier,F., *et al.* (2023) Germline pathogenic variants in HNRNPU are associated with alterations in blood methylome. *European Journal of Human Genetics*, 31, 1040–1047.
22. Yugami,M., Okano,H., Nakanishi,A. and Yano,M. (2020) Analysis of the nucleocytoplasmic shuttling RNA-binding protein HNRNPU using optimized HITS-CLIP method. *PLoS One*, 15.
23. Hendrickson,D., Kelley,D.R., Tenen,D., Bernstein,B. and Rinn,J.L. (2016) Widespread RNA binding by chromatin-associated proteins. *Genome Biol*, 17.

24. Van Nostrand,E.L., Pratt,G.A., Yee,B.A., Wheeler,E.C., Blue,S.M., Mueller,J., Park,S.S., Garcia,K.E., Gelboin-Burkhart,C., Nguyen,T.B., *et al.* (2020) Principles of RNA processing from analysis of enhanced CLIP maps for 150 RNA binding proteins. *Genome Biol*, 21.
25. Ma,G., Fu,X., Zhou,L., Babarinde,I.A., Shi,L., Yang,W., Chen,J., Xiao,Z., Qiao,Y., Ma,L., *et al.* (2025) The nuclear matrix stabilizes primed-specific genes in human pluripotent stem cells. *Nat Cell Biol*, 10.1038/s41556-024-01595-5.
26. Wen,Y., Ma,X., Wang,X., Wang,F., Dong,J., Wu,Y., Lv,C., Liu,K., Zhang,Y., Zhang,Z., *et al.* (2021) hnRNPU in Sertoli cells cooperates with WT1 and is essential for testicular development by modulating transcriptional factors Sox8/9. *Theranostics*, 11, 10030–10046.
27. Jurica,M.S., Licklider,L.J., Gygi,S.P., Grigorieff,N. and Moore,M.J. (2002) Purification and characterization of native spliceosomes suitable for three-dimensional structural analysis. *RNA*, 8(4), 426-39.
28. Uhlin,E., Rönnholm,H., Day,K., Kele,M., Tammimies,K., Bölte,S. and Falk,A. (2017) Derivation of human iPS cell lines from monozygotic twins in defined and xeno free conditions. *Stem Cell Res*, 18, 22–25.
29. Falk,A., Koch,P., Kesavan,J., Takashima,Y., Ladewig,J., Alexander,M., Wiskow,O., Tailor,J., Trotter,M., Pollard,S., *et al.* (2012) Capture of neuroepithelial-like stem cells from pluripotent stem cells provides a versatile system for in vitro production of human neurons. *PLoS One*, 7.
30. Chambers,S.M., Fasano,C.A., Papapetrou,E.P., Tomishima,M., Sadelain,M. and Studer,L. (2009) Highly efficient neural conversion of human ES and iPS cells by dual inhibition of SMAD signaling. *Nat Biotechnol*, 27, 275–280.
31. Li,Y., Collins,M., Geiser,R., Bakkar,N., Riascos,D. and Bowser,R. (2015) RBM45 homo-oligomerization mediates association with ALS-linked proteins and stress granules. *Sci Rep*, 5.
32. Martindale,J.L., Gorospe,M. and Idda,M.L. (2020) Ribonucleoprotein Immunoprecipitation (RIP) Analysis. *Bio Protoc*, 10.
33. Moggridge,S., Sorensen,P.H., Morin,G.B. and Hughes,C.S. (2018) Extending the Compatibility of the SP3 Paramagnetic Bead Processing Approach for Proteomics. *J Proteome Res*, 17, 1730–1740.
34. Shannon,P., Markiel,A., Ozier,O., Baliga,N.S., Wang,J.T., Ramage,D., Amin,N., Schwikowski,B. and Ideker,T. (2003) Cytoscape: A software Environment for integrated models of biomolecular interaction networks. *Genome Res*, 13, 2498–2504.
35. Liao,Y., Wang,J., Jaehnig,E.J., Shi,Z. and Zhang,B. (2019) WebGestalt 2019: gene set analysis toolkit with revamped UIs and APIs. *Nucleic Acids Res*, 47, W199–W205.
36. Yu,D., Chojnowski,G., Rosenthal,M. and Kosinski,J. (2023) AlphaPulldown—a python package for protein–protein interaction screens using AlphaFold-Multimer. *Bioinformatics*, 39.

37. Jumper,J., Evans,R., Pritzel,A., Green,T., Figurnov,M., Ronneberger,O., Tunyasuvunakool,K., Bates,R., Žídek,A., Potapenko,A., *et al.* (2021) Highly accurate protein structure prediction with AlphaFold. *Nature*, 596, 583–589.
38. Dobin,A., Davis,C.A., Schlesinger,F., Drenkow,J., Zaleski,C., Jha,S., Batut,P., Chaisson,M. and Gingeras,T.R. (2013) STAR: Ultrafast universal RNA-seq aligner. *Bioinformatics*, 29, 15–21.
39. Zhang,Z. and Xing,Y. (2017) CLIP-seq analysis of multi-mapped reads discovers novel functional RNA regulatory sites in the human transcriptome. *Nucleic Acids Res*, 45, 9260–9271.
40. Love,M.I., Huber,W. and Anders,S. (2014) Moderated estimation of fold change and dispersion for RNA-seq data with DESeq2. *Genome Biol*, 15.
41. Liao,Y., Smyth,G.K. and Shi,W. (2019) The R package Rsubread is easier, faster, cheaper and better for alignment and quantification of RNA sequencing reads. *Nucleic Acids Res*, 47.
42. Zhao,W., Zhang,S., Zhu,Y., Xi,X., Bao,P., Ma,Z., Kapral,T.H., Chen,S., Zagrovic,B., Yang,Y.T., *et al.* (2022) POSTAR3: An updated platform for exploring post-transcriptional regulation coordinated by RNA-binding proteins. *Nucleic Acids Res*, 50, D287–D294.
43. Skene,N.G. and Grant,S.G.N. (2016) Identification of vulnerable cell types in major brain disorders using single cell transcriptomes and expression weighted cell type enrichment. *Front Neurosci*, 10.
44. Polioudakis,D., de la Torre-Ubieta,L., Langerman,J., Elkins,A.G., Shi,X., Stein,J.L., Vuong,C.K., Nichterwitz,S., Gevorgian,M., Opland,C.K., *et al.* (2019) A Single-Cell Transcriptomic Atlas of Human Neocortical Development during Mid-gestation. *Neuron*, 103, 785-801.e8.
45. Kolberg,L., Raudvere,U., Kuzmin,I., Adler,P., Vilo,J. and Peterson,H. (2023) G:Profiler-interoperable web service for functional enrichment analysis and gene identifier mapping (2023 update). *Nucleic Acids Res*, 51, W207–W212.
46. Bailey,T.L., Johnson,J., Grant,C.E. and Noble,W.S. (2015) The MEME Suite. *Nucleic Acids Res*, 43, W39–W49.
47. Tsurusaki,Y., Okamoto,N., Ohashi,H., Mizuno,S., Matsumoto,N., Makita,Y., Fukuda,M., Isidor,B., Perrier,J., Aggarwal,S., *et al.* (2014) Coffin-Siris syndrome is a SWI/SNF complex disorder. *Clin Genet*, 85, 548–554.
48. Gennarino,V.A., Palmer,E.E., McDonell,L.M., Wang,L., Adamski,C.J., Koire,A., See,L., Chen,C.A., Schaaf,C.P., Rosenfeld,J.A., *et al.* (2018) A Mild PUM1 Mutation Is Associated with Adult-Onset Ataxia, whereas Haploinsufficiency Causes Developmental Delay and Seizures. *Cell*, 172, 924-936.e11.
49. Harel,T., Yoon,W.H., Garone,C., Gu,S., Coban-Akdemir,Z., Eldomery,M.K., Posey,J.E., Jhangiani,S.N., Rosenfeld,J.A., Cho,M.T., *et al.* (2016) Recurrent De Novo and Biallelic Variation of ATAD3A, Encoding a Mitochondrial Membrane Protein, Results in Distinct Neurological Syndromes. *Am J Hum Genet*, 99, 831–845.

50. Zhang,Z. and Xing,Y. (2017) CLIP-seq analysis of multi-mapped reads discovers novel functional RNA regulatory sites in the human transcriptome. *Nucleic Acids Res*, 45, 9260–9271.
51. Dixon,G., Pan,H., Yang,D., Rosen,B.P., Jashari,T., Verma,N., Pulecio,J., Caspi,I., Lee,K., Stransky,S., *et al.* (2021) QSER1 protects DNA methylation valleys from de novo methylation. *Science (1979)*, 372.
52. Barabási,A.L. and Oltvai,Z.N. (2004) Network biology: Understanding the cell's functional organization. *Nat Rev Genet*, 5, 101–113.
53. Caldu-Primo,J.L., Alvarez-Buylla,E.R. and Davila-Velderrain,J. (2018) Structural robustness of mammalian transcription factor networks reveals plasticity across development. *Sci Rep*, 8.
54. Gleeson JG, Lin PT, Flanagan LA, Walsh CA. (1999) Doublecortin Is a Microtubule-Associated Protein and Is Expressed Widely by Migrating Neurons. *Neuron*. 2, 257-71.
55. Hehr U, Uyanik G, Aigner L, Couillard-Despres S and Winkler J. *DCX*-Related Disorders. In: GeneReviews. Seattle (WA): University of Washington, Seattle; 1993–2025
56. Barber,M., Di Meglio,T., Andrews,W.D., Hernández-Miranda,L.R., Murakami,F., Chédotal,A. and Parnavelas,J.G. (2009) The role of Robo3 in the development of cortical interneurons. *Cerebral Cortex*, 19.
57. Wang,X., Xu,J., Li,Q., Zhang,Y., Lin,Z., Zhai,X., Wang,F., Huang,J., Gao,Q., Wen,J., *et al.* (2024) RNA-binding protein hnRNPU regulates multiple myeloma resistance to selinexor. *Cancer Lett*, 580.
58. Cho,J., Chang,H., Kwon,S.C., Kim,B., Kim,Y., Choe,J., Ha,M., Kim,Y.K. and Kim,V.N. (2012) LIN28A is a suppressor of ER-associated translation in embryonic stem cells. *Cell*, 151, 765–777.
59. Lee,E.K., Kim,H.H., Kuwano,Y., Abdelmohsen,K., Srikantan,S., Subaran,S.S., Gleichmann,M., Mughal,M.R., Martindale,J.L., Yang,X., *et al.* (2010) HnRNP C promotes APP translation by competing with FMRP for APP mRNA recruitment to P bodies. *Nat Struct Mol Biol*, 17, 732–739.
60. Hyder,Z., Van Paesschen,W., Sabir,A., Sansbury,F.H., Burke,K.B., Khan,N., Chandler,K.E., Cooper,N.S., Wright,R., McHale,E., *et al.* (2021) ERBB4 exonic deletions on chromosome 2q34 in patients with intellectual disability or epilepsy. *European Journal of Human Genetics*, 29, 1377–1383.
61. Aksoylu,I.S., Martin,P., Robert,F., Szkop,K.J., Redmond,N.E., Bhattacharyya,S., Wang,J., Chen,S., Beauchamp,R.L., Nobeli,I., *et al.* (2023) Translatome analysis of tuberous sclerosis complex 1 patient-derived neural progenitor cells reveals rapamycin-dependent and independent alterations. *Mol Autism*, 14.
62. Narayanan,R., Pham,L., Kerimoglu,C., Watanabe,T., Castro Hernandez,R., Sokpor,G., Ulmke,P.A., Kiszka,K.A., Tonchev,A.B., Rosenbusch,J., *et al.* (2018) Chromatin Remodeling BAF155 Subunit Regulates the Genesis of Basal Progenitors in Developing Cortex. *iScience*, 4, 109–126.

63. Bachmann,C., Nguyen,H., Rosenbusch,J., Pham,L., Rabe,T., Patwa,M., Sokpor,G., Seong,R.H., Ashery-Padan,R., Mansouri,A., *et al.* (2016) mSWI/SNF (BAF) Complexes Are Indispensable for the Neurogenesis and Development of Embryonic Olfactory Epithelium. *PLoS Genet*, 12.
64. Feng,J., Chang,H., Li,E. and Fan,G. (2005) Dynamic expression of de novo DNA methyltransferases Dnmt3a and Dnmt3b in the central nervous system. *J Neurosci Res*, 79, 734–746.
65. Sohni,A., Bartoccetti,M., Khoueiry,R., Spans,L., Vande Velde,J., De Troyer,L., Pulakanti,K., Claessens,F., Rao,S. and Koh,K.P. (2015) Dynamic Switching of Active Promoter and Enhancer Domains Regulates Tet1 and Tet2 Expression during Cell State Transitions between Pluripotency and Differentiation . *Mol Cell Biol*, 35, 1026–1042.
66. Veland,N., Hardikar,S., Zhong,Y., Gayatri,S., Dan,J., Strahl,B.D., Rothbart,S.B., Bedford,M.T. and Chen,T. (2017) The Arginine Methyltransferase PRMT6 Regulates DNA Methylation and Contributes to Global DNA Hypomethylation in Cancer. *Cell Rep*, 21, 3390–3397.
67. Jönsson,M.E., Ludvik Brattås,P., Gustafsson,C., Petri,R., Yudovich,D., Pircs,K., Verschuere,S., Madsen,S., Hansson,J., Larsson,J., *et al.* (2019) Activation of neuronal genes via LINE-1 elements upon global DNA demethylation in human neural progenitors. *Nat Commun*, 10.
68. Rhee,K.D., Yu,J., Zhao,C.Y., Fan,G. and Yang,X.J. (2012) Dnmt1-dependent DNA methylation is essential for photoreceptor terminal differentiation and retinal neuron survival. *Cell Death Dis*, 3.
69. Seyama,R., Tsuchida,N., Okada,Y., Sakata,S., Hamada,K., Azuma,Y., Hamanaka,K., Fujita,A., Koshimizu,E., Miyatake,S., *et al.* (2022) Two families with TET3-related disorder showing neurodevelopmental delay with craniofacial dysmorphisms. *J Hum Genet*, 67, 157–164.
70. Zhou,H., Yan,Y., Gao,J., Ma,M., Liu,Y., Shi,X., Zhang,Q. and Xu,X. (2023) Heterogeneous Nuclear Protein U Degraded the m 6 A Methylated TRAF3 Transcript by YTHDF2 To Promote Porcine Epidemic Diarrhea Virus Replication . *J Virol*, 97.
71. Liu,J., Dou,X., Chen,C., Chen,C., Liu,C., Michelle Xu,M., Zhao,S., Shen,B., Gao,Y., Han,D., *et al.* (2020) N6-methyladenosine of chromosome-associated regulatory RNA regulates chromatin state and transcription. *Science (1979)*, 367, 580–586.
72. Deng,S., Zhang,J., Su,J., Zuo,Z., Zeng,L., Liu,K., Zheng,Y., Huang,X., Bai,R., Zhuang,L., *et al.* (2022) RNA m6A regulates transcription via DNA demethylation and chromatin accessibility. *Nat Genet*, 54, 1427–1437.
73. Liu,N., Dai,Q., Zheng,G., He,C., Parisien,M. and Pan,T. (2015) N6 -methyladenosine-dependent RNA structural switches regulate RNA-protein interactions. *Nature*, 518, 560–564.